RSC Advances

PAPER

View Article Online
View Journal | View Issue

Cite this: *RSC Adv.*, 2017, **7**, 45369

Superior photocatalytic performance of $LaFeO_3$/g-C_3N_4 heterojunction nanocomposites under visible light irradiation

Ke Xu[ab] and Jian Feng *[b]

Received 7th August 2017
Accepted 11th September 2017

DOI: 10.1039/c7ra08715b

rsc.li/rsc-advances

New types of $LaFeO_3$/g-C_3N_4 heterostructures were successfully prepared and the enhanced photocatalytic hydrogen evolution and degradation activities under visible light irradiation were determined. They possessed the features of a Z-scheme photocatalysis system. The photoexcited electrons on the conduction band of $LaFeO_3$ were transferred to the valence band of g-C_3N_4 by the solid–solid intimately contacted interfaces, where the electrons and holes were recombined, and thus improved the separation of photogenerated electrons and holes of g-C_3N_4. The $LaFeO_3$/g-C_3N_4 heterostructures showed a higher hydrogen evolution rate and a higher amount of $^{\bullet}OH$ than pure $LaFeO_3$ and g-C_3N_4. The construction of the $LaFeO_3$/g-C_3N_4 heterostructures was used to demonstrate an effective strategy for improving the photocatalytic property. The 5%-$LaFeO_3$/g-C_3N_4 exhibited the highest photodegradation and water splitting rate. More than 95% of methylene blue (MB) was degraded after 15 min in the presence of 25 mg EDTA-2Na in 100 mL MB solution which was irradiated using a 3 W light-emitting diode. The 5%-$LaFeO_3$/g-C_3N_4 heterojunction nanocomposite had a maximum hydrogen evolution rate of 158 μmol g^{-1} h^{-1}.

1. Introduction

The rapid development of modern industry using the consumption of non-renewable fossil fuels has caused a serious global energy shortage and environmental pollution.[1] As the largest renewable energy source, the exploitation of solar energy could mean less use of fossil fuels and thereby protect the environment. The utilization of solar energy using semiconductor-based photocatalysis has the capability of hydrogen (H_2) evolution and pollutant removal, and is considered as an economical, renewable, clean and safe technology. A variety of semiconductor photocatalysts have been developed over the past few decades.[2–5] Because visible light energy accounts for more than 40% of the sunlight energy, people are committed to developing visible light driven photocatalysts. So far, various visible light responsive semiconductor photocatalysts have been developed,[6–9] but the fast charge recombination and insufficient stability still make it impractical for general use.

Very recently, graphitic carbon nitride (g-C_3N_4) was found to be a promising metal-free material with a large surface area, high thermal and chemical stability, fast charge transfer rate, and a suitable bandgap of approximately 2.7 eV.[10–13] It is consequently regarded as the next generation photocatalyst for water splitting and degradation of pollutants under visible light irradiation. However, the low photocatalytic efficiency of g-C_3N_4 caused by its narrow response range to visible light, fast recombination of photogenerated electron–hole pairs and low quantum efficiency limits its further applications. Therefore, researchers have focussed on different modification methods to improve its photocatalytic activity, including copolymerization,[14] morphology control[15] and doping.[16] The construction of the g-C_3N_4–semiconductor heterostructures is an effective strategy to promote the separation of a photogenerated electron and hole, and thus improve the photocatalytic property.

A variety of nanocomposites have been reported in the literature for dye degradation and H_2 evolution. Halogenides,[17,18] sulfides[19,20] and oxides[21,22] have been developed to construct the heterojunction with g-C_3N_4. These g-C_3N_4–semiconductor heterostructures possess excellent photocatalytic performance in degradation of organic pollutants. Fu *et al.*[17] reported novel heterojunctions of bismuth oxybromide–carbon nitride (BiOBr–C_3N_4) fabricated by depositing BiOBr nanoflakes onto the surface of C_3N_4. The optimum photocatalytic activity of the 0.5BiOBr–0.5C_3N_4 heterojunction was 4.9 and 17.2 times as high as those of individual BiOBr and C_3N_4, respectively, under visible light irradiation. Jiang *et al.*[20] synthesized calcium indium sulfide ($CaIn_2S_4$)/g-C_3N_4 heterojunction nanocomposites using a two-step method. It exhibited a H_2 evolution rate of 102 μmol g^{-1} h^{-1}, which was more than 3 times that of

[a]*Department of Biochemistry, Guizhou Education University, 115 Gaoxin Road, Guiyang, Guizhou, 550018, China*

[b]*Department of Chemistry, School of Basic Medical Science, Guizhou Medical University, 9 Beijing Road, Guiyang, Guizhou, 550004, China. E-mail: jfeng@gmc.edu.cn*

pristine $CaIn_2S_4$. The highest activity was obtained for a 30% $CaIn_2S_4$/g-C_3N_4 heterojunction nanocomposite, over which 90% of methyl orange was degraded after 120 min. Zhao *et al.*[21] prepared novel g-C_3N_4/tz-$Bi_{0.92}Gd_{0.08}VO_4$ heterojunctions using a microwave hydrothermal method. The degradation rate of Rhodamine B was 94% after 20 min, which was 39.97% higher than that of g-C_3N_4. All the g-C_3N_4/tz-$Bi_{0.92}Gd_{0.08}VO_4$ heterojunctions exhibited a higher degradation rate than that of the pure one. These g-C_3N_4–semiconductor heterostructures possess excellent photocatalytic performance in degradation of organic pollutants. However, there are only a few reports in the literature involving g-C_3N_4-based heterostructures with simultaneously enhanced photocatalytic degradation and H_2 evolution performance.

Perovskite lanthanum ferric oxide ($LaFeO_3$) has been applied to catalysts, sensors, environmental monitoring and membranes in syngas production.[23,24] $LaFeO_3$ exhibits an interesting catalytic activity in the degradation of chlorinated volatile organic compounds.[25] $LaFeO_3$ has a band gap of about 2.0 eV, which is advantageous for absorbing visible light, for good thermal stability and for high catalytic activity.[26] In this work, $LaFeO_3$/g-C_3N_4 Z-scheme photocatalysis system was constructed. The photoexcited electrons on the conduction band (CB) of $LaFeO_3$ were transferred to the valence band (VB) of g-C_3N_4 by the solid–solid intimately contacted interfaces, where the electrons and holes were recombined, and thus improved the separation of the photogenerated electron and hole of g-C_3N_4. Combining this with a sacrificial agent [triethanolamine (TEOA) or ethylenediaminetetraacetic acid disodium salt (EDTA-2Na)] which reacted with the holes on the VB of $LaFeO_3$, the photocatalytic efficiency was improved significantly. The $LaFeO_3$/g-C_3N_4 Z-scheme photocatalysis system showed a higher H_2 evolution rate and a higher amount of $^{\cdot}OH$ than pure $LaFeO_3$ and g-C_3N_4. More than 95% of methylene blue (MB) was degraded after 15 min in the presence of 25 mg EDTA-2Na in 100 mL MB solution irradiated using a 3 W light-emitting diode (LED). The 5%-$LaFeO_3$/g-C_3N_4 heterojunction nanocomposite had a maximum H_2 evolution rate of 158 μmol g^{-1} h^{-1}.

2. Experimental

2.1 Chemicals

Iron(III) nitrate nonahydrate ($Fe(NO_3)_3$), lanthanum(III) nitrate hexahydrate ($La(NO_3)_3$) hexachloroplatinic acid (H_2PtCl_6), terephthalic acid, MB and melamine were purchased from Shanghai Aladdin Biochemical Technology Co., Ltd. All the chemicals were used without further purification.

2.2 Preparation of $LaFeO_3$/g-C_3N_4

Graphitic carbon nitride was prepared by the polycondensation of melamine (6 g) at 500 °C for 4 h in a muffle furnace. The ramping rate was 2 °C min^{-1}. For a typical synthetic reaction of the $LaFeO_3$/g-C_3N_4 nanocomposites, 2 g of g-C_3N_4, 0.1700 g of $Fe(NO_3)_3$, and 0.1800 g of $La(NO_3)_3$ were dissolved in 50 mL of deionized water (H_2O) with stirring for 1 h. Then, the solution was evaporated to generate a solid product which was then ground into powder. The powder was placed in a crucible with a cover and then heated for another 2 h at 450 °C in a muffle furnace. The $LaFeO_3$/g-C_3N_4 nanocomposites were obtained after cooling down the powder to room temperature. The as-prepared product was 5%-$LaFeO_3$/g-C_3N_4. Changing the amounts of $Fe(NO_3)_3$, and $La(NO_3)_3$ added, 10%, 20%, 40% and 60% nanocomposites were synthesized. The as-prepared $LaFeO_3$/g-C_3N_4 containing 5, 10, 20, 40, 60 wt% of $LaFeO_3$ were denoted as LF1-5 or 5%-$LaFeO_3$/g-C_3N_4 and so on.

2.3 Characterization

Transmission electron microscopy (TEM) and high-resolution-TEM (HRTEM) images were performed on a FEI Tecnai G2 F20 transmission electron microscope. X-ray diffraction patterns (XRD) patterns were carried out on a Rigaku D/Max 2500 X-ray diffractometer with Cu Kα radiation ($\lambda = 1.5406$ Å). X-ray photoelectron spectroscopy (XPS) was carried out using an ESCA PHI500 spectrometer. Infrared spectra were obtained using a Nicolet NEXUS 470 Fourier-transform infrared spectroscopy (FTIR) instrument in the range of 4000–500 cm^{-1}. Ultraviolet-visible (UV-vis) spectra were recorded on a Varian Cary 50 spectrophotometer. UV-vis diffuse reflectance spectra (DRS) were measured on Shimadzu UV-2401 spectrophotometer equipped with a spherical diffuse reflectance accessory.

2.4 Photoelectrochemical measurement

A portion of photocatalyst (8 mg; g-C_3N_4, $LaFeO_3$ or $LaFeO_3$/g-C_3N_4), 2 mL of ethanol and 40 μL of 5 wt% Nafion were mixed to form a slurry. Then the suspension was dropped onto fluorine doped tin oxide (FTO) glass with an area of 1 cm^2 which performed as the working electrode in a three-electrode system. Platinum (Pt) foil was selected as auxiliary electrode, and silver/silver chloride (Ag/AgCl) as reference electrode. A 3 W LED lamp was the light source. The photocurrent was measured in 0.2 M aqueous solution of sodium sulfate.

2.5 Photocatalytic degradation of MB

The photocatalytic activities of photocatalysts (g-C_3N_4, $LaFeO_3$ or $LaFeO_3$/g-C_3N_4) were determined in a 5 mg L^{-1} aqueous solution of MB. For a typical photodegradation process, 100 mg of photocatalyst was dispersed in 100 mL of MB solution with magnetic stirring in dark for 30 min to reach an adsorption–desorption equilibrium. Then the photodegradation was tested under 3 W LED irradiation. A portion (5 mL) of reaction mixture was collected at the certain time intervals and centrifuged to remove the photocatalyst. The absorption peak at 664 nm was chose to determine the concentration of MB using a Varian Cary 50 spectrophotometer.

2.6 Measurement of hydroxyl radicals

A 0.5 mM solution of terephthalic acid (TA) was obtained by dissolving TA in 2.0 mM sodium hydroxide. Then 100 mg photocatalyst was suspended in 100 mL of TA solution. The mixture was then irradiated under 3 W LED irradiation. A

portion (5 mL) of reaction mixture was collected at the certain time intervals and then centrifuged. The fluorescence intensity of 2-hydroxyterephthalic acid (HTA) was measured on a PerkinElmer LS 55 luminescence spectrometer.

2.7 Photocatalytic hydrogen evolution

The photocatalytic H_2 evolution reactions were implemented in an irradiation reaction vessel with a Pyrex top connected to a glass closed gas circulation system. Photocatalyst (100 mg) (g-C_3N_4, $LaFeO_3$ or $LaFeO_3$/g-C_3N_4) was dispersed in 200 mL of an aqueous solution containing 10 vol% TEOA. Pt (3 wt%) as a cocatalyst was deposited on the photocatalysts using an *in situ* photodeposition approach using H_2PtCl_6. The reaction temperature was kept at 20 °C. The H_2 concentration was monitored using a Unisense microsensor monometer equipped with a Clark-type electrochemical H_2 microsensor. The light source was a 300 W xenon (Xe) lamp with a 400 nm longpass cutoff filter.

3. Results and discussion

The XRD patterns of g-C_3N_4, $LaFeO_3$ and $LaFeO_3$/g-C_3N_4 heterojunction nanocomposites are presented in Fig. 1. The g-C_3N_4 sample exhibited two diffraction peaks at 13.2° and 27.5°, corresponding to (100) and (002) diffraction planes, respectively. All the diffraction peaks of $LaFeO_3$ were indexed to an orthorhombic phase (PDF#37-1493), indicating the purity and high crystallinity of $LaFeO_3$. After forming the $LaFeO_3$/g-C_3N_4 heterojunction nanocomposites with g-C_3N_4, only the XRD pattern of 5%-$LaFeO_3$/g-C_3N_4 was similar to that of g-C_3N_4. Other $LaFeO_3$/g-C_3N_4 nanocomposites simultaneously maintained the features of pure g-C_3N_4 and $LaFeO_3$. With the increase of $LaFeO_3$ content in the nanocomposites, diffraction peaks originating from g-C_3N_4 were gradually decreased. These XRD results proved the formation of the $LaFeO_3$/g-C_3N_4 composites.

TEM images of the 5%-$LaFeO_3$/g-C_3N_4 nanocomposites are shown in Fig. 2. The g-C_3N_4 exhibited a thin and irregular nanosheet structure with wrinkles (Fig. 2a).[20] The $LaFeO_3$ nanoparticles with a diameter of about 30 nm were distributed in g-C_3N_4 to form a heterostructure with interfacial contact. This heterostructure could effectively improve the photocatalytic activity by supplying plenty of reactive sites to adsorb reactant and capture charge carriers. The representative particle in the selected region displayed continuous lattice fringes with a *d*-spacing of 0.2480 nm, corresponding to the (201) planes of the orthorhombic phase of $LaFeO_3$ (Fig. 2c–e).

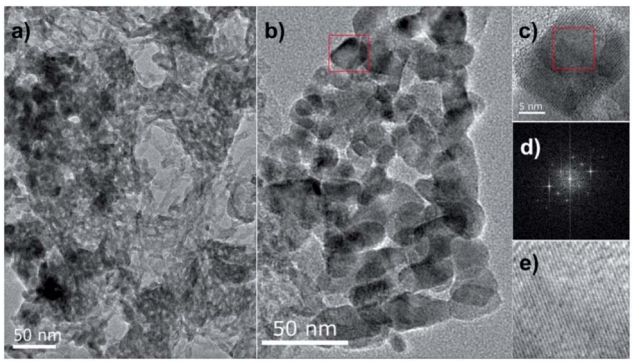

Fig. 2 TEM images (a, b) and HRTEM micrograph (c) of the selected area image of 5%-$LaFeO_3$/g-C_3N_4, with the fast Fourier transform (FTT) pattern (d) and the corresponding inverse FFT pattern (e).

Fig. 3a displays the FTIR spectra of g-C_3N_4, $LaFeO_3$ and $LaFeO_3$/g-C_3N_4. The broad absorption peak centered at 3200 cm^{-1} and the peak at 1640 cm^{-1} in the spectra of g-C_3N_4 and $LaFeO_3$/g-C_3N_4 were assigned to the stretching and bending vibrations of N–H. With the increase of $LaFeO_3$ content in the $LaFeO_3$/g-C_3N_4 nanocomposites, the intensities of these two absorption peaks were gradually decreased and ultimately disappeared. Fig. 3b shows the corresponding magnification of FTIR spectra in the range of 650 cm^{-1} to 1800 cm^{-1}. The absorption at 810 cm^{-1} was derived from the breathing vibration of *s*-triazine. The absorption peaks at 1575, 1413, 1326 and 1249 cm^{-1} were ascribed to characteristic C–N stretching of the g-C_3N_4 heterocycles.[20,27] The decrease of the intensities revealed the reduced content of g-C_3N_4. However, for 40%-$LaFeO_3$/g-C_3N_4 and 60%-$LaFeO_3$/g-C_3N_4, these characteristic absorption peaks had disappeared in the same way as for $LaFeO_3$. Combined with the XRD results, these results suggested that the 5%-$LaFeO_3$/g-C_3N_4, 10%-$LaFeO_3$/g-C_3N_4 and 20%-$LaFeO_3$/g-C_3N_4 samples contained two components of $LaFeO_3$ and g-C_3N_4.

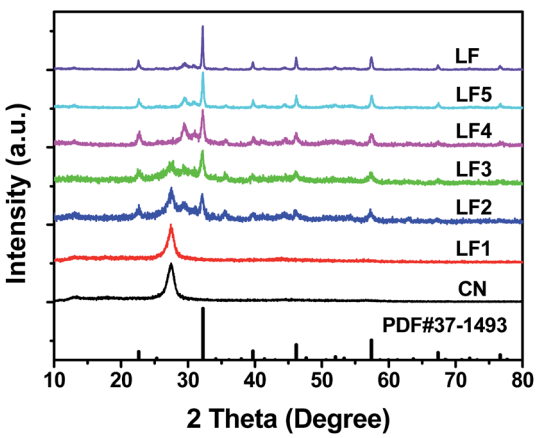

Fig. 1 XRD patterns of g-C_3N_4 (CN), $LaFeO_3$ (LF) and $LaFeO_3$/g-C_3N_4 (LF1–LF5).

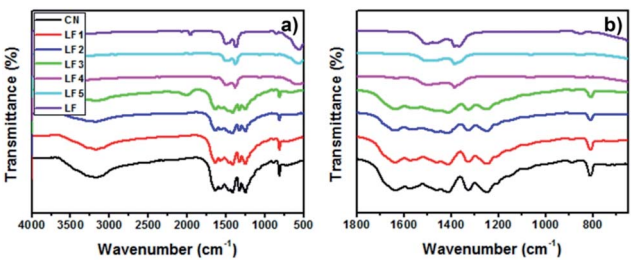

Fig. 3 (a) FTIR spectra of g-C_3N_4, $LaFeO_3$ and $LaFeO_3$/g-C_3N_4 and (b) the corresponding magnification from 650 cm^{-1} to 1800 cm^{-1}.

Fig. 4a shows the XPS survey spectra of 5%-$LaFeO_3$/g-C_3N_4, which proves the presence of carbon (C), iron (Fe), lanthanum (La), nitrogen (N), and oxygen (O), in the nanocomposite. Fig. 4b–f shows the corresponding high resolution spectra of the C 1s, N 1s, Fe 2p, La 3d and O 1s orbitals. The N 1s peak at 398.43 eV was a characteristic peak allocated to sp^2 hybridized nitrogen (C=N–C).[17,22] The peak at 399.96 eV was attributed to the tertiary nitrogen and amino groups with an H atom. In the C 1s spectra, two peaks at 284.82 and 287.98 eV were derived from contaminated carbon on the surface of $LaFeO_3$/g-C_3N_4 sample and sp^2 C atoms bonded to amino groups in the triazine cycles. The N 1s and C 1s spectra confirmed the presence of the g-C_3N_4. The peak of Fe 2p3/2 and Fe 2p1/2 at 711.1 and 724.9 eV, respectively, were assigned to the core level spectra of Fe^{3+} in its oxide form.[28,29] Two La 3d peaks at 836.2 and 852.3 eV were identified as spin–orbit splitting of 3d5/2 and 3d3/2 of La^{3+}, respectively, in the oxide.[30] For O 1s spectra, only one peak at 531.6 eV was observed and was ascribed to the oxygen network in the perovskite lattice of $LaFeO_3$. The binding energy of O 1s, Fe 2p and La 3d for 5%-$LaFeO_3$/g-C_3N_4 shifted to higher values. However, the peaks of N 1s and C 1s shifted to lower binding energies. These shifts of binding energies demonstrated that g-C_3N_4 was covered closely on the surface of $LaFeO_3$, and showed a strong chemical interaction between g-C_3N_4 and $LaFeO_3$.[22]

The UV-vis DRS of g-C_3N_4, $LaFeO_3$ and $LaFeO_3$/g-C_3N_4 with different $LaFeO_3$ contents are shown in Fig. 5a. Pure g-C_3N_4 displayed an absorption edge at 455 nm, corresponding to a band gap energy (E_g) of 2.73 eV (Fig. 5b), which was consistent

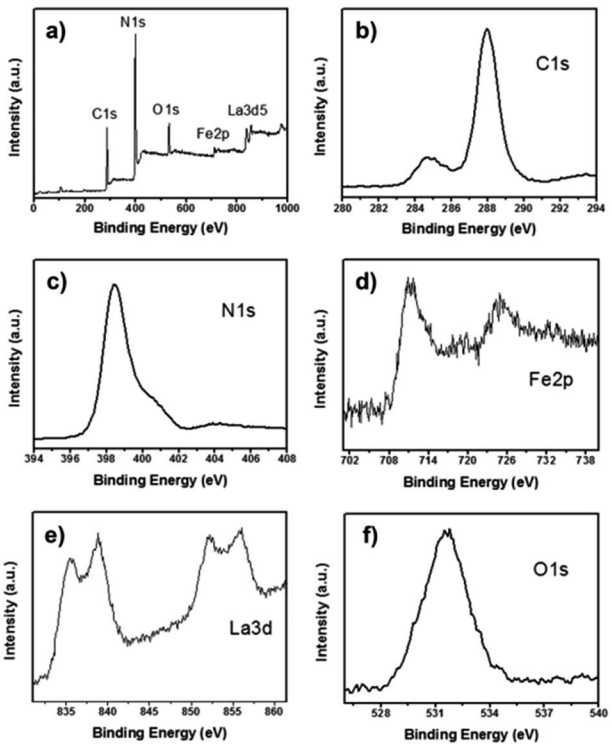

Fig. 4 (a) Survey XPS spectra and high resolution spectra of C (b), N (c), Fe (d), La (e) and O (f) of 5%-$LaFeO_3$/g-C_3N_4.

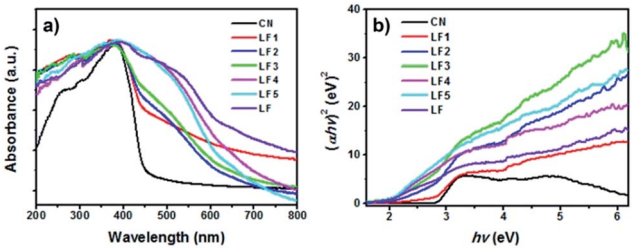

Fig. 5 (a) UV-vis DRS spectra and (b) band gap energies of pure g-C_3N_4, $LaFeO_3$ and $LaFeO_3$/g-C_3N_4 heterojunctions.

with previous results found in the literature.[31] $LaFeO_3$ showed a strong light absorption in the range of 200 to 800 nm. $LaFeO_3$/g-C_3N_4 samples had broader absorptions and longer absorption edge wavelengths than that of g-C_3N_4, which was attributed to the strong interaction between $LaFeO_3$ and g-C_3N_4 in the heterostructures.

The band gap energies of g-C_3N_4, $LaFeO_3$ and $LaFeO_3$/g-C_3N_4 were calculated using the Tauc relationship. Fig. 5b shows the Tauc plots of $(ahv)^2$ *versus* hv.[32] The band gap energies of g-C_3N_4 and $LaFeO_3$ were 2.73 and 1.92 eV, respectively. The E_g of $LaFeO_3$ was slightly smaller than the reported values found in the literature (2.0 eV).[33] The E_g values of $LaFeO_3$/g-C_3N_4 with different $LaFeO_3$ content from 5% to 60% were 2.69, 2.55, 2.45, 1.92 and 1.92 eV. These results indicated that the E_g reduced as the $LaFeO_3$ content increased from 5% to 20%. However, the 40%-$LaFeO_3$/g-C_3N_4 and 60%-$LaFeO_3$/g-C_3N_4 had the same E_g values as pure $LaFeO_3$. It was suggested that $LaFeO_3$ and g-C_3N_4 had not formed the heterostructures in 40%-$LaFeO_3$/g-C_3N_4 and 60%-$LaFeO_3$/g-C_3N_4 samples efficiently, which was also demonstrated by the XRD and FTIR results. The most probable causes proposed are given next. In this work, 60% or 40% of g-C_3N_4 was heated with iron nitrate and lanthanum nitrate for 2 h at 450 °C to prepare the samples. This heat treatment procedure could give rise to volatilization of g-C_3N_4, which decreased the actual amounts of g-C_3N_4 in the samples. The relative higher $LaFeO_3$ content and lack of g-C_3N_4 lead to self-agglomeration of $LaFeO_3$, and consequently the heterostructures could not be formed efficiently.

The CB and VB edge positions of the g-C_3N_4 and $LaFeO_3$ were calculated using the following two equations:

$$E_{VB} = X - E_e + 0.5E_g$$

$$E_{CB} = E_{VB} - E_g$$

where E_{VB}, X, E_e, E_{CB} represented the VB edge potential, the absolute electronegativity, the energy of free electrons on the H_2 scale (4.5 eV) and the CB edge potential, respectively. The E_g was obtained from the UV-vis DRS. The E_{VB} and E_{CB} were 1.54 and −1.28 eV for g-C_3N_4, and 2.03 and 0.11 eV for $LaFeO_3$, which were similar to the reported E_{VB} and E_{CB} of +1.57 and −1.12 eV for g-C_3N_4 (ref. 32) and 2.115 and 0.025 eV for $LaFeO_3$.[23]

To test the photocatalytic activity of the $LaFeO_3$/g-C_3N_4 heterojunctions, photocatalytic degradation of MB under 3 W LED irradiation was implemented. The absorption peak at 664 nm

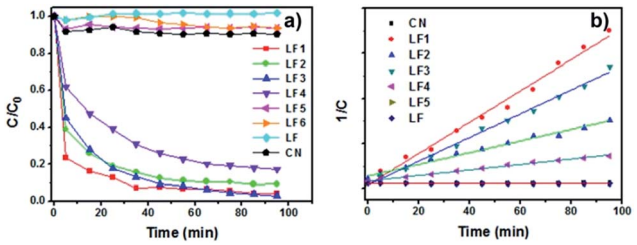

Fig. 6 (a) Photocatalytic degradation of MB over g-C_3N_4, $LaFeO_3$ and $LaFeO_3$/g-C_3N_4 under 3 W LED irradiation and (b) corresponding second-order kinetics plots.

was selected to monitor the degradation of MB. As shown in Fig. 6a, only 3–10% of MB was degraded over the g-C_3N_4, $LaFeO_3$ and 60%-$LaFeO_3$/g-C_3N_4 under 3 W LED irradiation for 120 min. By comparison, the degradation rate of MB on the $LaFeO_3$/g-C_3N_4 samples with 5%, 10% and 20% $LaFeO_3$ was significantly enhanced. The 5%-$LaFeO_3$/g-C_3N_4 heterojunction exhibited the highest photocatalytic activity, over which more than 95% of MB was degraded after irradiation for 120 min.

The second-order kinetics model was used to fit the photocatalytic degradation data. The results are shown in Fig. 6b. The 5%-$LaFeO_3$/g-C_3N_4 heterojunction nanocomposite exhibited the highest photocatalytic activity. Its second-order reaction rate constant was around 49.7 and 86.9 times more than pure g-C_3N_4 and $LaFeO_3$ (Fig. 7), respectively. On the basis of the previous XRD, FTIR and DRS measurements, this photocatalytic degradation result demonstrated that $LaFeO_3$ and g-C_3N_4 had effectively formed the heterojunction composites. The strong interfacial interaction between $LaFeO_3$ and g-C_3N_4 in the composites could improve the transfer of the photoproduced charge and enhance their photocatalytic performances.[17] This strong interfacial interaction between $LaFeO_3$ and g-C_3N_4 in the composites was investigated using simple mechanical mixing of $LaFeO_3$ and g-C_3N_4 in the same ratio as the composites and then using it to degrade MB under 3 W LED irradiation (curve LF6 in Fig. 6a). The photocatalytic activity of the 5%-$LaFeO_3$/g-C_3N_4 heterojunction nanocomposite was much higher than that of a simple mechanical mixture. This result indicated the formation of intimately contacted interfaces in the heterojunction nanocomposite, which is also displayed in the TEM images (Fig. 2).

The stability of the 5%-$LaFeO_3$/g-C_3N_4 heterojunction nanocomposite was studied by recycling 5%-$LaFeO_3$/g-C_3N_4 under the same photocatalytic degradation conditions for degrading MB. As shown in Fig. 8a, after four recycles, no significant changes were observed. This result proved that the $LaFeO_3$/g-C_3N_4 nanocomposites possessed a relatively high stability for photocatalytic degradation of MB.

These photocatalytic degradation results revealed that the intimately contacted interfaces between $LaFeO_3$ and g-C_3N_4 in the heterojunction nanocomposite resulted in the high transfer and separation of photoproduced charges at the interface of the heterostructures.[17] This assumption was further confirmed by the transient photocurrent responses of the g-C_3N_4, $LaFeO_3$ and 5%-$LaFeO_3$/g-C_3N_4. The photocurrent–time (I–t) curves were obtained by intermittently cutting off the visible light irradiation (Fig. 8b). The photocurrent value of 5%-$LaFeO_3$/g-C_3N_4 was about two times higher than pure $LaFeO_3$ and g-C_3N_4. This was attributed to the efficient separation of the photoproduced charges in space and consequently reduced the carrier recombination.

To investigate which type of reactive species, including hydrogen peroxide (H_2O_2), h^+, e^-, $^{\bullet}OH$ and $^{\bullet}O_2^-$, were involved in the photocatalytic degradation of MB over the 5%-$LaFeO_3$/g-C_3N_4, ammonium oxalate (AO), EDTA-2Na, isopropanol (IPA), NO_3^-, catalase (CAT) and benzoquinone (BQ) were added to the degradation solutions.[34] AO and EDTA-2Na were the scavenger of h^+, IPA was the scavenger of $^{\bullet}OH$ radicals, NO_3^- acted as the e^- scavenger, CAT was the H_2O_2 scavenger, and BQ acted as the $^{\bullet}O_2^-$ radical scavenger. As shown in Fig. 9a, no obvious changes were found when NO_3^- and CAT were added to the solutions, indicating that e^- and H_2O_2 were not the active species in the photocatalytic degradation of MB. The addition of IPA significantly decreased the photodegradation rate. It was revealed that $^{\bullet}OH$ radicals were the dominant species for MB photodegradation. As shown in Fig. 9a, BQ also decreased the photodegradation rate slightly, demonstrating the minor role of $^{\bullet}O_2^-$. However, in the presence of AO and EDTA-2Na, the photocatalytic degradation rate was remarkably increased. Only a few reports in the literature have reported the increase of photodegradation rate by the addition of EDTA-2Na in to the solution.[35,36] It was considered that the addition of EDTA-2Na

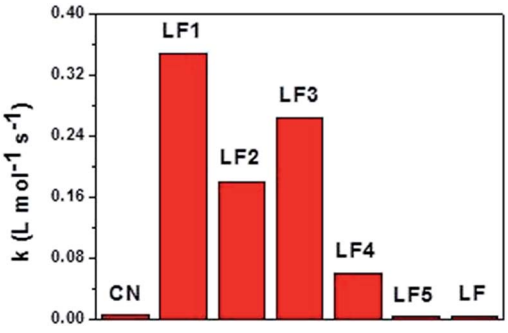

Fig. 7 The second-order reaction rate constants of photocatalytic degradation of MB on g-C_3N_4, $LaFeO_3$ and $LaFeO_3$/g-C_3N_4 under 3 W LED irradiation.

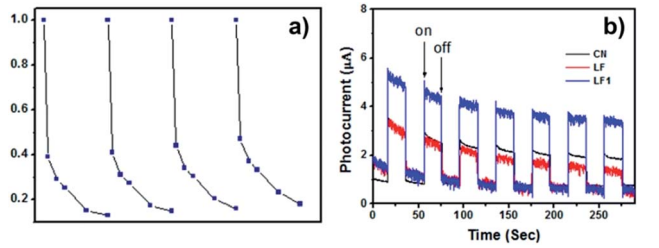

Fig. 8 (a) Stability study of photocatalytic degradation of MB over the 5%-$LaFeO_3$/g-C_3N_4 heterojunction under 3 W LED irradiation, and (b) transient photocurrent responses of the g-C_3N_4, $LaFeO_3$ and 5%-$LaFeO_3$/g-C_3N_4 heterojunction.

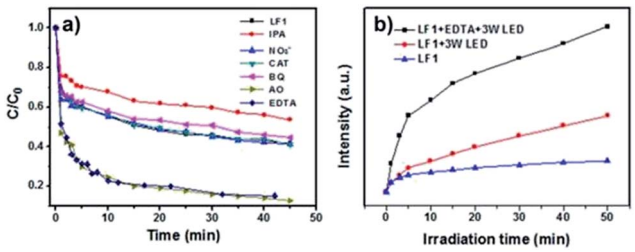

Fig. 9 (a) C/C_0 variation of the photocatalytic degradation of MB over the 5%-$LaFeO_3$/g-C_3N_4 in the presence of different scavengers under 3 W LED irradiation, and (b) HTA fluorescence intensities over the 5%-$LaFeO_3$/g-C_3N_4 monitored at the peak of 424 nm under 3 W LED irradiation or under indoor light irradiation.

trapped the h^+ and promoted the separation rate of the e^-/h^+ pairs, and consequently more $^{\cdot}OH$ radicals were achieved. Therefore the photodegradation activity was improved.

To confirm the increase of $^{\cdot}OH$ radicals in the presence of EDTA-2Na, TA was used to react with $^{\cdot}OH$ to form 2-hydroxyterephthalic acid (HTA), which possessed strong fluorescence.[17,37] The results of the HTA experiment are shown in Fig. 9b. It shows that the peak intensities of HTA were enhanced significantly when EDTA-2Na was added in to the degradation solution. Fig. 9b also revealed that more $^{\cdot}OH$ radicals were generated under 3 W LED irradiation than were produced under indoor light irradiation. Different dosages of EDTA-2Na were added to the degradation solution to test the influence of EDTA-2Na concentration on the photodegradation of MB over the 5%-$LaFeO_3$/g-C_3N_4. The results are shown in Fig. 10. It indicated that by increasing the amount of EDTA-2Na, the photocatalytic degradation rate was enhanced dramatically. More than 95% of MB was degraded by adding 25 mg EDTA-2Na to 100 mL MB solution and then irradiated with a 3 W LED for 15 min.

The photocatalytic H_2 evolution activity of g-C_3N_4, $LaFeO_3$ and $LaFeO_3$/g-C_3N_4 heterojunctions in aqueous solution containing 10 vol% TEOA under 300 W Xe lamp irradiation were studied. As shown in Fig. 11, the H_2 evolution rate was negligible over the pure $LaFeO_3$, g-C_3N_4, 40%-$LaFeO_3$/g-C_3N_4 and 60%-$LaFeO_3$/g-C_3N_4. The photocatalytic H_2 evolution activity of

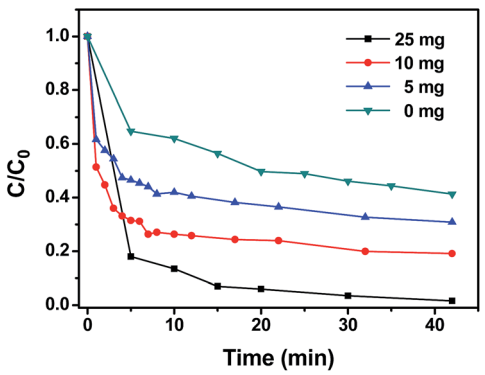

Fig. 10 The influence of different dosages of EDTA-2Na on the photodegradation of MB over the 5%-$LaFeO_3$/g-C_3N_4 with 3 W LED irradiation.

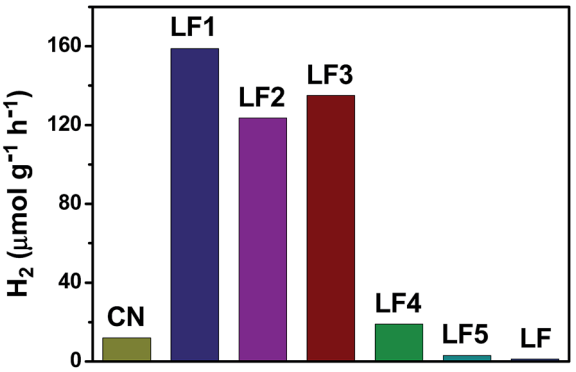

Fig. 11 The photocatalytic hydrogen evolution activity under 300 W Xe lamp irradiation over g-C_3N_4, $LaFeO_3$ and $LaFeO_3$/g-C_3N_4 nanocomposites.

$LaFeO_3$/g-C_3N_4 containing 5, 10 and 20 wt% of $LaFeO_3$ was remarkably enhanced. The 5%-$LaFeO_3$/g-C_3N_4 heterojunction nanocomposite in particular had a maximum H_2 evolution rate of 158 μmol g^{-1} h^{-1}.

The recyclability of 5%-$LaFeO_3$/g-C_3N_4 nanocomposites was tested using five cycles of photocatalytic H_2 evolution under identical reaction conditions. As shown in Fig. 12, 450 μmol of H_2 was generated after irradiation for 3 h under visible light in the first run. The amount of H_2 was finally reduced to 395 μmol in the fifth run. Only 12.2% H_2 production was lost after the fifth photocatalytic experiment. The results indicated that 5%-$LaFeO_3$/g-C_3N_4 was quite stable for photocatalytic H_2 production under visible light irradiation.

On the basis of the results of the $^{\cdot}OH$ trapping experiments, the potential route of chemical reactions responsible for the generation of $^{\cdot}OH$ was determined. The photocatalytic procedure over $LaFeO_3$/g-C_3N_4 was in accordance with the features of a Z-scheme photocatalysis system. Under visible light irradiation, both $LaFeO_3$ and g-C_3N_4 were excited to obtain photoinduced electron and hole pairs. The photoexcited electrons of $LaFeO_3$ and g-C_3N_4 transited from the VB to the CB and the holes were left on the VB. The electrons from the CB of $LaFeO_3$

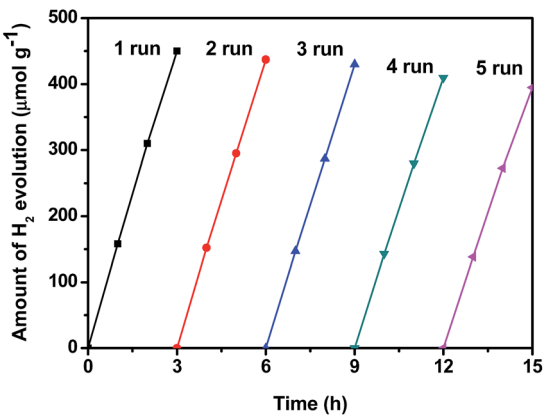

Fig. 12 Recyclability of the H_2 evolution test over 5%-$LaFeO_3$/g-C_3N_4 nanocomposites under 300 W Xe lamp irradiation.

transferred to the VB of g-C_3N_4 using the solid–solid intimately contacted interfaces, where the electrons and holes were recombined and thus improved the separation of the photogenerated electrons and holes of g-C_3N_4. Then the excited electrons reduced O_2 adsorbed on the surface of g-C_3N_4 to produce $^{\bullet}O_2^-$. The $^{\bullet}O_2^-$ reacted with H_2O to achieve $^{\bullet}OH$. Finally, MB was degraded by $^{\bullet}OH$ and $^{\bullet}O_2^-$. As shown in Fig. 13, the CB edge potential of $LaFeO_3$ was more positive than the standard redox potential of H^+/H_2, which cannot reduce H^+ to form H_2. H^+ was subsequently reduced by the CB electrons of g-C_3N_4 to generate H_2. The holes on the VB of $LaFeO_3$ reacted with TEOA or EDTA-2Na (as the sacrificial agent) to promote the separation of the photogenerated electrons and holes, which resulted in the improvement of the photocatalytic performance.

The photocatalytic H_2 evolution activity was consistent with the photodegradation rate of MB. The excess $LaFeO_3$ (above 20 wt% in the nanocomposite) decreased the H_2 evolution rate. Fig. 13 clearly shows the correlation between the higher H_2 evolution rate and higher amount of $^{\bullet}OH$ generated over the $LaFeO_3$/g-C_3N_4 heterojunction nanocomposites. It possessed the features of a Z-scheme system. Under visible light irradiation, both $LaFeO_3$ and g-C_3N_4 were excited to obtain photoinduced electron and hole pairs. The photoexcited electrons of $LaFeO_3$ and g-C_3N_4 transited from the VB to the CB and the holes were left on the VB. The electrons from the CB of $LaFeO_3$ were transferred to the VB of g-C_3N_4 by the solid–solid intimately contacted interfaces, where the electrons and holes were recombined and thus improved the separation of the photogenerated electrons and holes of g-C_3N_4. Then the excited electrons on the CB of g-C_3N_4 efficiently generated the $^{\bullet}OH$. Meanwhile, the improved separation of the photogenerated electron and hole of g-C_3N_4 of this Z-scheme system also efficiently enhanced the H_2 evolution rate. The holes on the VB of $LaFeO_3$ reacted with TEOA or EDTA-2Na (as the sacrificial agent) to promote the separation of photogenerated electrons and holes, which resulted in the improvement of the photocatalytic performance.

The results revealed that the optimum concentration of $LaFeO_3$ was 5 wt% for the maximum photocatalytic H_2 evolution and photodegradation rate. Too high a content of $LaFeO_3$ was adverse for the efficacious formation of heterojunction nanocomposites and also gave reduced photocatalytic H_2 evolution and photodegradation rate. $LaFeO_3$ and g-C_3N_4 did not form efficiently the heterostructures in 40%-$LaFeO_3$/g-C_3N_4 and 60%-$LaFeO_3$/g-C_3N_4 samples, which was demonstrated by the XRD and FTIR results. This led to the 40%-$LaFeO_3$/g-C_3N_4 and 60%-$LaFeO_3$/g-C_3N_4 samples having a much lower degradation rate.

5%-$LaFeO_3$/g-C_3N_4, 10%-$LaFeO_3$/g-C_3N_4 and 20%-$LaFeO_3$/g-C_3N_4 formed intimately contacted interfaces in the nanocomposites, which had higher degradation rate. Among these nanocomposites, 5%-$LaFeO_3$/g-C_3N_4 gave the optimum results for MB degradation. The absorption edges of g-C_3N_4, $LaFeO_3$ and $LaFeO_3$/g-C_3N_4 are compared in Fig. 5a. This revealed that $LaFeO_3$/g-C_3N_4 samples had broader absorptions and longer absorption edge wavelengths than that of g-C_3N_4. The absorption intensity of 5%-$LaFeO_3$/g-C_3N_4 in the visible light region was much higher than that of 10%-$LaFeO_3$/g-C_3N_4 and 20%-$LaFeO_3$/g-C_3N_4, which indicated that the 5%-$LaFeO_3$/g-C_3N_4 produced a greater amount of photogenerated electron–hole pairs.[34] Based on the UV-vis DRS spectra, XRD and FTIR results, it could be deduced that the greater amount of photogenerated electron–hole pairs and the efficient charge separation of the Z-scheme photocatalytic system gave the 5%-$LaFeO_3$/g-C_3N_4 heterojunction, the highest MB degradation and H_2 evolution rate.

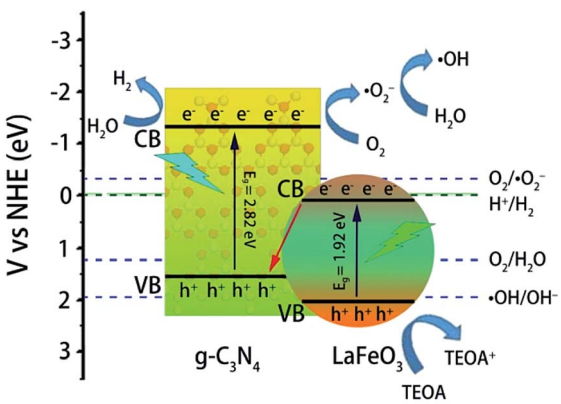

Fig. 13 Possible photocatalytic degradation of MB and H_2 evolution mechanism over $LaFeO_3$/g-C_3N_4 heterojunctions under visible light irradiation.

4. Conclusion

The new type of $LaFeO_3$/g-C_3N_4 heterostructures were successfully prepared using a two-step method. It possessed the features of a Z-scheme photocatalysis system. The photoexcited electrons on the CB of $LaFeO_3$ were transferred to the VB of g-C_3N_4 by the solid–solid intimately contacted interfaces, where the electrons and holes were recombined and thus improved the separation of photogenerated electrons and holes of g-C_3N_4. $LaFeO_3$ and g-C_3N_4 also effectively formed intimately contacted interfaces. This strong interfacial interaction could improve the transfer photoproduced charge and enhance their photocatalytic performances. Thus, $LaFeO_3$/g-C_3N_4 heterostructures had a higher H_2 evolution rate and a higher amount of $^{\bullet}OH$ than pure $LaFeO_3$ and g-C_3N_4. The construction of $LaFeO_3$/g-C_3N_4 heterostructures was demonstrated to be the effective strategy to improve the photocatalytic property. The 5%-$LaFeO_3$/g-C_3N_4 exhibited the highest photodegradation and water splitting rate. More than 95% of MB was degraded after 15 min in the presence of 25 mg EDTA-2Na in 100 mL of MB solution with irradiation using a 3 W LED. The photogenerated $^{\bullet}OH$ radicals were the main oxidative species for the degradation of MB. Its second-order reaction rate constant was about 49.7 and it was 86.9 times more than that of pure g-C_3N_4 and $LaFeO_3$. The 5%-$LaFeO_3$/g-C_3N_4 heterojunction nanocomposite had a maximum H_2 evolution rate of 158 μmol g^{-1} h^{-1}. This research shows an easy approach to manufacturing $LaFeO_3$/g-C_3N_4 heterojunction nanocomposites to promote the exploitation of solar energy.

Conflicts of interest

There are no conflicts to declare.

Acknowledgements

This research was supported by the Science and Technology Foundation of Guizhou, China (No. [2013] 2044, No. [2015] 7338, No. [2016] 7366), and the Science and Technology Foundation of Guiyang, China (No. [20161001] 001).

Notes and references

1 S. Cao, J. Low, J. Yu and M. Jaroniec, *Adv. Mater.*, 2015, **27**, 2150.
2 A. Fujishima and K. Honda, *Nature*, 1972, **238**, 37.
3 J. Yu, J. Low, W. Xiao, P. Zhou and M. Jaroniec, *J. Am. Chem. Soc.*, 2014, **136**, 8839.
4 X. Wang, M. Liao, Y. Zhong, J. Y. Zheng, W. Tian, T. Zhai, C. Zhi, Y. Ma, J. Yao, Y. Bando and D. Golberg, *Adv. Mater.*, 2012, **24**, 3421.
5 W. C. Huang, L. M. Lyu, Y. C. Yang and M. H. Huang, *J. Am. Chem. Soc.*, 2012, **134**, 1261.
6 Z. Zou, J. Ye, K. Sayama and H. Arakawa, *Nature*, 2001, **414**, 625.
7 M. Liu, W. You, Z. Lei, G. Zhou, J. Yang, G. Wu, G. Ma, G. Luan, T. Takata, M. Hara, K. Domen and C. Li, *Chem. Commun.*, 2004, 2192.
8 Y. Hu, X. Gao, L. Yu, Y. Wang, J. Ning, S. Xu and X. W. Lou, *Angew. Chem., Int. Ed.*, 2013, **52**, 5636.
9 X. Zhou, Q. Xu, W. Lei, T. Zhang, X. Qi, G. Liu, K. Deng and J. Yu, *Small*, 2014, **10**, 674.
10 Y. Wang, X. Wang and M. Antonietti, *Angew. Chem., Int. Ed.*, 2012, **51**, 68.
11 E. Kroke, *Angew. Chem., Int. Ed.*, 2014, **53**, 11134.
12 A. Thomas, A. Fischer, F. Goettmann, M. Antonietti, J. Müller, R. Schlöglb and J. M. Carlssonc, *J. Mater. Chem.*, 2008, **18**, 4893.
13 Y. Zheng, J. Liu, J. Liang, M. Jaroniecc and S. Z. Qiao, *Energy Environ. Sci.*, 2012, **5**, 6717.
14 J. Zhang, X. Chen, K. Takanabe, K. Maeda, K. Domen, J. D. Epping, X. Fu, M. Antonietti and X. Wang, *Angew. Chem., Int. Ed.*, 2010, **49**, 441.
15 Y. Zheng, L. Lin, X. Ye, F. Guo and X. Wang, *Angew. Chem., Int. Ed.*, 2014, **53**, 11926.
16 G. Liu, P. Niu, C. Sun, S. C. Smith, Z. Chen, G. Q. Lu and H. Cheng, *J. Am. Chem. Soc.*, 2010, **132**, 11642.
17 J. Fu, Y. Tian, B. Chang, F. Xi and X. Dong, *J. Mater. Chem.*, 2012, **22**, 21159.
18 S. Yang, W. Zhou, C. Ge, X. Liu, Y. Fang and Z. Li, *RSC Adv.*, 2013, **3**, 5631.
19 W. Tian, Q. Shen, N. Li and J. Zhou, *RSC Adv.*, 2016, **6**, 25568.
20 D. Jiang, J. Li, C. Xing, Z. Zhang, S. Meng and M. Chen, *ACS Appl. Mater. Interfaces*, 2015, **7**, 19234.
21 C. Zhao, G. Tan, J. Huang, W. Yang, H. Ren and A. Xia, *ACS Appl. Mater. Interfaces*, 2015, **7**, 23949.
22 F. Li, S. Liu, Y. Xue, X. Wang, Y. Hao, J. Zhao, R. Liu and D. Zhao, *Chem.–Eur. J.*, 2015, **21**, 10149.
23 J. Yang, R. Hu, W. Meng and Y. Du, *Chem. Commun.*, 2016, **52**, 2620.
24 P. Li, X. Hu, L. Zhang, H. Dai and L. Zhang, *Nanoscale*, 2011, **3**, 974.
25 X. Ren, H. Yang, S. Gen, J. Zhou, T. Yang, X. Zhang, Z. Cheng and S. Sun, *Nanoscale*, 2016, **8**, 752.
26 Q. Yu, X. Meng, T. Wang, P. Li, L. Liu, K. Chang, G. Liu and J. Ye, *Chem. Commun.*, 2015, **51**, 3630.
27 L. M. Sun, Y. Qi, C. J. Jia, Z. Jin and W. L. Fan, *Nanoscale*, 2014, **6**, 2649.
28 M. Markova-Velichkova, T. Lazarova, V. Tumbalev, G. Ivanov, D. Kovacheva, P. Stefanov and A. Naydenov, *Chem. Eng. J.*, 2013, **231**, 236.
29 H. Wu, R. Hu, T. Zhou, C. Li, W. Meng and J. Yang, *CrystEngComm*, 2015, **17**, 3859.
30 S. Thirumalairajan, K. Girija, N. Y. Hebalkar, D. Mangalaraj, C. Viswanathan and N. Ponpandian, *RSC Adv.*, 2013, **3**, 7549.
31 H. Zhang, L. Guo, L. Zhao, B. Wan and Y. Yang, *J. Phys. Chem. Lett.*, 2015, **6**, 958.
32 H. Liu, Z. Jin, Z. Xu, Z. Zhang and D. Ao, *RSC Adv.*, 2015, **5**, 97951.
33 L. Jing, Y. Qu, H. Su, C. Yao and H. Fu, *J. Phys. Chem. C*, 2011, **115**, 12375.
34 H. Li, Y. Liu, X. Gao, C. Fu and X. Wang, *ChemSusChem*, 2015, **8**, 1189.
35 S. Hu, L. Ma, J. You, F. Li, Z. Fan, F. Wang, D. Liu and J. Gui, *RSC Adv.*, 2014, **4**, 21657.
36 J. Zhang, S. Hu and Y. Wang, *RSC Adv.*, 2014, **4**, 62912.
37 R. Marschall, A. Mukherji, A. Tanksale, C. Sun, S. C. Smith, L. Wang and G. Q. Lu, *J. Mater. Chem.*, 2011, **21**, 8871.

